nanomaterials

MDPI

Article

Enhanced Thermoelectric Performances of CNTs-Reinforced Cement Composites with $Bi_{0.5}Sb_{1.5}Te_3$ for Pavement Energy Harvesting

Hongyu Zhou *, Huang Liu, Guoping Qian *, Peng Xu, Huanan Yu, Jun Cai and Jianlong Zheng

National Engineering Laboratory for Highway Maintenance Technology, School of Traffic and Transportation Engineering, Changsha University of Science and Technology, Changsha 410114, China
* Correspondence: zhouhongyu23@126.com (H.Z.); guopingqian@sina.com (G.Q.)

Abstract: Driven by the huge thermal energy in cement concrete pavements, thermoelectric (TE) cement has attracted considerable attention. However, the current TE cement shows poor performance, which greatly limits its application. Herein, a series of $Bi_{0.5}Sb_{1.5}Te_3$/carbon nanotubes (CNTs) co-reinforced cement composites have been prepared, and their TE properties were systematically investigated. It was shown that the addition of $Bi_{0.5}Sb_{1.5}Te_3$ particles can effectively improve the TE properties of CNTs-reinforced cement composites by building a better conductive network, increasing energy filtering and interfaces scattering. The $Bi_{0.5}Sb_{1.5}Te_3$/CNTs cement composites with 0.6 vol.% of $Bi_{0.5}Sb_{1.5}Te_3$ exhibits the highest ZT value of 1.2×10^{-2}, increased by 842 times compared to that of the CNTs-reinforced cement composites without $Bi_{0.5}Sb_{1.5}Te_3$. The power output of this sample with the size of $2.5 \times 3.5 \times 12$ mm^3 reaches 0.002 μW at a temperature difference of 19.1 K. These findings shed new light on the development of high-performance TE cement, which can guide continued advances in their potential application of harvesting thermal energy from pavements.

Keywords: $Bi_{0.5}Sb_{1.5}Te_3$; CNTs; cement; thermoelectric performances; energy harvesting

check for updates

Citation: Zhou, H.; Liu, H.; Qian, G.; Xu, P.; Yu, H.; Cai, J.; Zheng, J. Enhanced Thermoelectric Performances of CNTs-Reinforced Cement Composites with $Bi_{0.5}Sb_{1.5}Te_3$ for Pavement Energy Harvesting. *Nanomaterials* **2022**, *12*, 3883. https://doi.org/10.3390/nano12213883

Academic Editor: Gyaneshwar P. Srivastava

Received: 12 October 2022
Accepted: 31 October 2022
Published: 3 November 2022

1. Introduction

Cement is one of the most abundantly produced and basic structural materials, which is widely used in infrastructures, including roads, bridges and buildings [1–3]. Due to the low heat dissipation rate of cement, the cement-related infrastructures store large-scale thermal energy after exposure to a large quantity of sun irradiation [4,5]. This results in structural damage in the cement-related infrastructures [6], the growing intensity of urban heat island effect and increasing energy consumption of the air conditioning system in summer [7,8].

In fact, one of the best choices is using thermoelectric (TE) materials to convert large-scale thermal energy into green electricity via Seebeck effect [9–12]. It is well known that the performance of a TE material relies on the dimensionless figure of merit $ZT = \sigma\alpha^2T/\kappa$, where σ, α, κ, and T are the electrical conductivity, Seebeck coefficient, thermal conductivity, and absolute temperature, respectively [13]. Good TE cement should possess high ZT value to improve the conversion capability from heat to electricity. Therefore, it is of significance to maximize the ZT value by enhancing the electrical transport properties (σ and α) and reducing thermal transport properties (κ). From the discovery of the Seebeck effect in carbon-fiber-reinforced concrete [14], numerous research studies have been carried out to explore various high ZT cement-based functional TE materials [15–21]. Unfortunately, the performances of most kinds of TE cement are less than 1.0×10^{-5} due to the poor electrical transport properties of the cement matrix.

Using carbon nanotubes (CNTs) as functional additives can significantly increase the electrical conductivity of cement because of their super σ and better conductive channel [22,23]. The σ of cement with 1 wt.% CNTs possessed a theoretical value of 3 S/m, increased by about 3000 times that of the cement without CNTs [24]. However, its α is primitive [25]. Wei et al. investigated the effect of functional additives (e.g., carbon materials [26,27] and metallic oxide [28,29]) on the TE performance of cement and found that the nano-metallic oxide increased the α. Liu et al. [30] discovered that forming a better electric conductive path was found to be very effective in tuning the σ of Bi_2Te_3 and carbon-fiber-reinforced cement composites. Ghosh et al. [31] reported that a graphene and ZnO nanoparticle double doping method can simultaneously increases the σ and α of cement composites. The relatively high α is due to the quantum confinement effect of the nanostructured ZnO. Besides, the κ of TE materials with multi-scale architecture is lower due to the phonon scattering at grain boundaries [32–34]. Therefore, the combination of multi-additives and multi-scale architecture could further improve TE performance.

Herein, we choose CNTs and multi-scale $Bi_{0.5}Sb_{1.5}Te_3$ particles as co-reinforced phase in cement composites, taking into account that $Bi_{0.5}Sb_{1.5}Te_3$ is the commercial *p*-type TE materials near room temperature. Remarkably, it has many attractive features, such as excellent σ, considerably large α and low κ [35]. It demonstrates that optimizing the $Bi_{0.5}Sb_{1.5}Te_3$ contents can not only enhance the σ values of cement composites by forming a shorter conductive network, but can also adjust α and κ via the enhanced scattering with multi-scale $Bi_{0.5}Sb_{1.5}Te_3$ particles. As a result, the largest ZT value of $Bi_{0.5}Sb_{1.5}Te_3$/CNTs co-reinforced cement composites with 0.6% $Bi_{0.5}Sb_{1.5}Te_3$ reaches 1.2×10^{-2} at 400 K, increased by 842 times compared to that of the CNTs-reinforced cement composites without $Bi_{0.5}Sb_{1.5}Te_3$. We also present the power generation performance of the optimized $Bi_{0.5}Sb_{1.5}Te_3$/CNTs co-reinforced cement composites. The results introduce a new promotion of the TE cement application for harvesting green electricity from pavement.

2. Materials and Methods

2.1. Raw Materials

Highly pure metals Bi (99.999%, powder), Sb (99.9%, powder) and Te (99.999%, powder) (Aladdin Biochemical Technology Co., Ltd., Shanghai, China) were used as starting materials to prepare the multi-scale $Bi_{0.5}Sb_{1.5}Te_3$ particles. CNTs (purity > 90%, SSA > 80 m^2/g, electrical conductivity = 69.7 S/cm) (Aladdin Biochemical Technology Co., Ltd., Shanghai, China) were used as conductive phase with lengths of 10–20 μm. Melamine sulfonated polycondensate (F10), hydroxyethyl cellulose (HEC), polyethylene glycol compound (P803), and silica fume (Shanghai Qinhe Chemical Co., Ltd., Shanghai, China) were employed as a water reducer, dispersant, defoamer, and active agent, respectively. Cement (P.O 42.5R) (Zhucheng Yangchun Cement Co., Ltd., Shangdong, China) was used as a matrix. Tap water was utilized as experimental solvent. No aggregate was taken.

2.2. Preparation of $Bi_{0.5}Sb_{1.5}Te_3$/CNTs Cement Composites

The process for producing $Bi_{0.5}Sb_{1.5}Te_3$/CNTs cement composites was as follows.

First, multi-scale $Bi_{0.5}Sb_{1.5}Te_3$ particles were prepared via the melt-quenching and grounding method; the detailed process was reported elsewhere [36].

Second, multi-scale $Bi_{0.5}Sb_{1.5}Te_3$ particles and CNTs were treated by ultrasonic dispersion for 20 minimums in water to obtain $Bi_{0.5}Sb_{1.5}Te_3$/CNTs dispersion. After that, cement, active agent, water reducer, dispersant, and defoamer were added into the dispersion, and then mixed by the mechanical stirrer of 10 minimums to form $Bi_{0.5}Sb_{1.5}Te_3$/CNTs cement pastes. The weights of CNTs, water, active agent, water reducer, dispersant, and defoamer to cement were fixed at 1:1000, 1:2, 1:20, 1:200, 6:1000, and 1:2000. The doping content of multi-scale $Bi_{0.5}Sb_{1.5}Te_3$ particles was controlled at the volume fractions of 0, 0.2, 0.4, 0.6, 0.8, and 1.0 vol.% to cement, respectively. Proportions for the cement pastes are listed in Table 1.

Table 1. The proportions of $Bi_{0.5}Sb_{1.5}Te_3$, CNTs, water, active agent, water reducer, dispersant, defoamer, and cement in the cement pastes.

	$Bi_{0.5}Sb_{1.5}Te_3$ Volume Fractions (vol.%)	Weight (g)	CNTs (g)	Water (g)	Active Agent (g)	Water Reducer (g)	Dispersant (g)	Defoamer (g)	Cement (g)
B1	0.0	0.0	0.01	5	0.5	0.05	0.06	0.005	10
B2	0.2	0.043	0.01	5	0.5	0.05	0.06	0.005	10
B3	0.4	0.086	0.01	5	0.5	0.05	0.06	0.005	10
B4	0.6	0.129	0.01	5	0.5	0.05	0.06	0.005	10
B5	0.8	0.173	0.01	5	0.5	0.05	0.06	0.005	10
B6	1.0	0.216	0.01	5	0.5	0.05	0.06	0.005	10

Final, the prepared cement pastes were poured into a polytetrafluoroethylene die and compacted with a vibrator to obtain dense $Bi_{0.5}Sb_{1.5}Te_3$/CNTs co-reinforced cement composites. Then, the demolded samples were cured in air at the relative humidity of about 95% for 28 days. To eliminate the effects of pore solution on the TE properties, all $Bi_{0.5}Sb_{1.5}Te_3$/CNTs cement composites were dried at 105 °C for 12 h after curing.

2.3. Characterization and Measurement

The constituent phases of the samples were determined by powder X-ray diffraction (XRD, PANalytical X' Pert PR) using the Cu K_α radiation (λ = 0.15418 nm). The microstructures and chemical compositions were analyzed by using scanning electron microscopy (SEM, TESCAN Mira4) and electron probe micro-analyzer (EPMA, JEOL JXA-8230).

The σ, α, work voltage (V), currents (I), and power output (P) of the as-prepared $Bi_{0.5}Sb_{1.5}Te_3$/CNTs cement composites were measured by a self-made equipment, as shown in Figure 1.

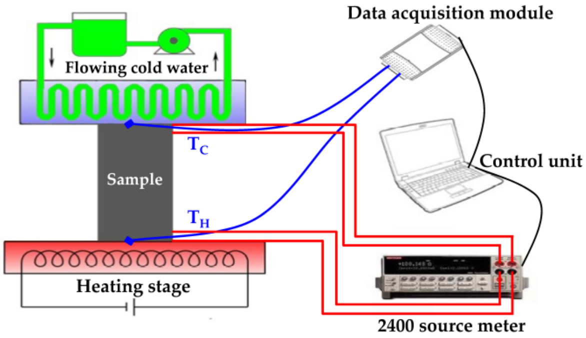

Figure 1. The schematic of self-made equipment for measuring properties of as-prepared samples.

The σ was given by using the equation $\sigma = IL/VS$, where L, S are the length and cross-sectional area of samples. The α was defined as $\alpha = \Delta V/\Delta T$, where ΔV, ΔT are the open circuit voltages and temperature difference of two sides. $\Delta T = T_H - T_C$, where T_H and T_C are the hot-side and cold-side temperature. The P was calculated by using the equation $P = VI$. The V, ΔV and I were measured by the Source Meter instrument (SMI, Keithley 2400). The hot-side temperature (T_H) and cold-side temperature (T_C) were recorded by a data-acquisition module, as shown in Figure 1. During σ measurements, the T_H and T_C were fixed, and the SMI instrument was set to different workloads to measure the I and V. It was evaluated by using the two outer thermocouples for temperature (T) measurement and the inner electrodes for open circuit voltages (ΔV) measurement. During α measurements, the T_H and T_C were controlled by the heating stage and flowing cold water. When the heating stage and the flowing cold water started working, the $\Delta T = T_H - T_C$ increased. Meanwhile, the SMI instrument was connected to the samples to measure the ΔV. Thus, the σ, α, V, I, and P were obtained.

The κ was calculated using the equation $\kappa = \lambda\rho C_p$, where λ is the thermal diffusivity coefficient, C_p is the specific heat capacity, and ρ is the bulk density of the material. The λ was measured using a laser-flash technique (Netzsch LFA-427) with the circular block in a flowing Ar atmosphere. The C_p was measured using a Q20 differential scanning calorimeter. The ρ was obtained via the standard Archimedes method.

3. Results

3.1. Composition and Structure Characterization

Figure 2a shows the SEM image of CNTs. It is obvious that the CNTs display a tubular structure. Diameter distribution of CNTs reveals normal distribution. The average diameter of CNTs is approximately 27 nm (Figure 2b). From the XRD pattern of CNTs (Figure 2c), it can be seen that all the diffraction peaks of CNTs can be indexed to the JCPDS 75-2078 file for C, which reveals that the powder is comprised of single-phase CNTs. Figure 2d and the inset of Figure 2e show the SEM image of the $Bi_{0.5}Sb_{1.5}Te_3$ powders. It shows that the multi-scale $Bi_{0.5}Sb_{1.5}Te_3$ particles have a wide size distribution from nm to µm. The corresponding average grain size obtained from Figure 2d is approximately 7.8 µm (Figure 2e). The XRD pattern of the $Bi_{0.5}Sb_{1.5}Te_3$ powder shows all the diffraction peaks of the $Bi_{0.5}Sb_{1.5}Te_3$ powders, which can be indexed to the JCPDS 49-1713 file for $Bi_{0.5}Sb_{1.5}Te_3$ (Figure 2f). This indicates that the single phase $Bi_{0.5}Sb_{1.5}Te_3$ has been successfully prepared.

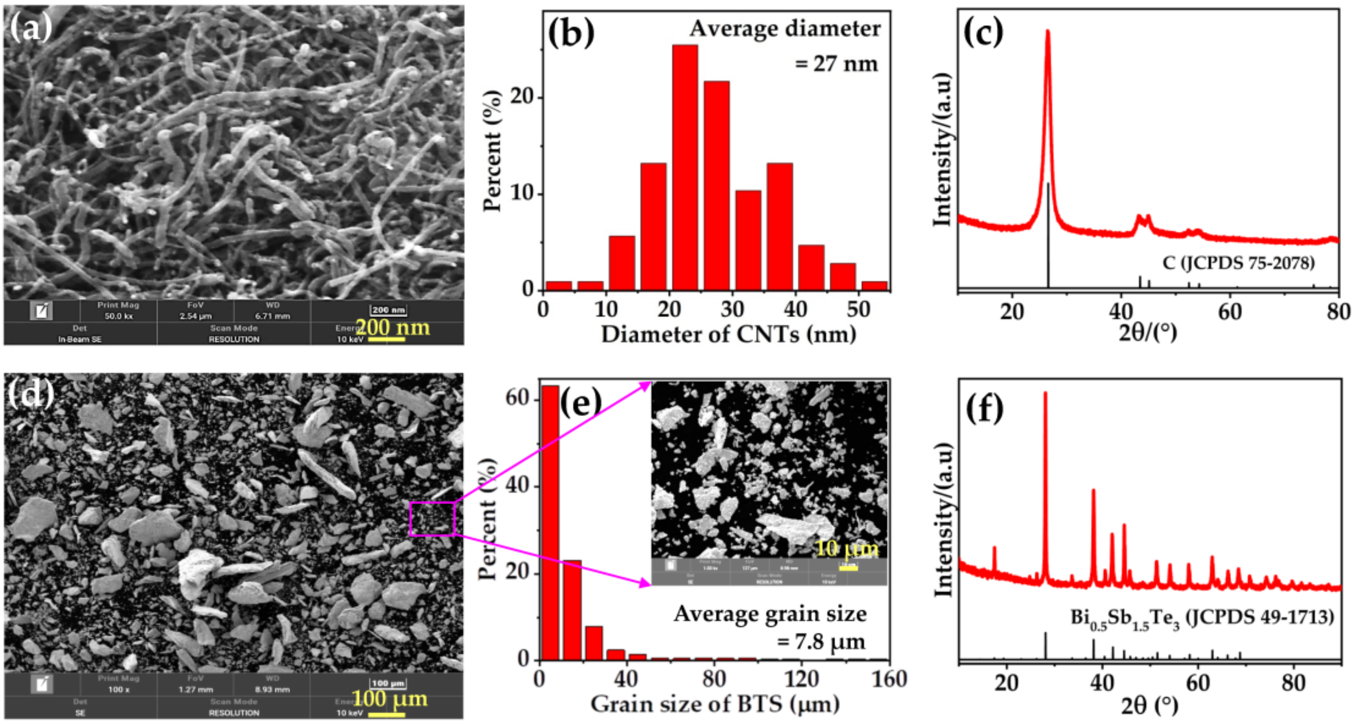

Figure 2. SEM images of (**a**) CNTs and (**d**) as-prepared $Bi_{0.5}Sb_{1.5}Te_3$ powders. The corresponding size distributions, which were statistically analyzed from SEM images of (**a**,**d**), are shown along with (**b**,**e**), respectively. XRD pattern of them are also shown in (**c**) CNTs, and (**f**) as-prepared $Bi_{0.5}Sb_{1.5}Te_3$ powders. The inset in (**e**) is the enlarged SEM image of (**d**).

Figure 3 displays the XRD patterns of $Bi_{0.5}Sb_{1.5}Te_3$/CNTs cement composites with different $Bi_{0.5}Sb_{1.5}Te_3$ contents. It can be seen that all samples consist of portlandite ($Ca(OH)_2$), ettringite (AFt), calcium silicate hydrate (C-S-H gel), alite (C_3S), belite (C_2S) and quartz (SiO_2). However, the diffraction peaks of $Bi_{0.5}Sb_{1.5}Te_3$ and CNTs are not detected, because their content is lower than the detection limit of the XRD method.

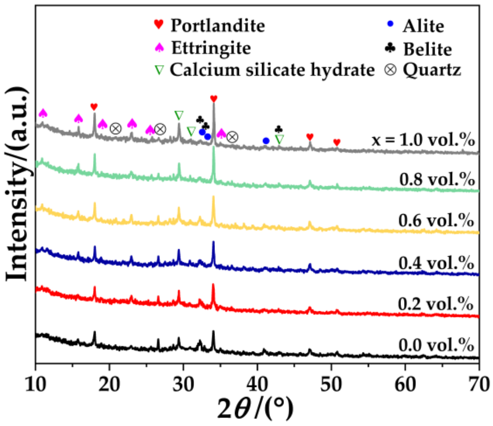

Figure 3. XRD patterns of $Bi_{0.5}Sb_{1.5}Te_3$/CNTs cement composites with different $Bi_{0.5}Sb_{1.5}Te_3$ contents.

It is noted that the intensities of the peaks relating to portlandite, ettringite, calcium silicate hydrate, alite, belite, and silica change. The main peak intensities of portlandite at 18.1°, 34.1° increase with the increasing contents of $Bi_{0.5}Sb_{1.5}Te_3$. The same trends of other hydrated products (ettringite, calcium silicate hydrate) are also shown in $Bi_{0.5}Sb_{1.5}Te_3$/CNTs cement composites, whereas the peak intensities of non-hydrated products (alite, belite and quartz) gradually decrease with the increasing contents of $Bi_{0.5}Sb_{1.5}Te_3$, indicating that multi-scale $Bi_{0.5}Sb_{1.5}Te_3$ particles may accelerate the hydration of $Bi_{0.5}Sb_{1.5}Te_3$/CNTs cement composites. Similar results can be found in Ref. [37].

Figure 4 displays the BEI photographs of the $Bi_{0.5}Sb_{1.5}Te_3$/CNTs cement composites. It can be seen that the brightest objects are multi-scale $Bi_{0.5}Sb_{1.5}Te_3$ particles and the darkest objects are CNTs. More multi-scale $Bi_{0.5}Sb_{1.5}Te_3$ particles appear when the contents of $Bi_{0.5}Sb_{1.5}Te_3$ increase from 0.0 vol.% to 1.0 vol.%. Significantly, the CNTs are dispersed uniformly for the samples at lower $Bi_{0.5}Sb_{1.5}Te_3$ contents, but accumulate together for the samples with the 0.8 vol.% and 1.0 vol.% $Bi_{0.5}Sb_{1.5}Te_3$, implying that higher $Bi_{0.5}Sb_{1.5}Te_3$ particles content (≥0.8 vol.%) may cause a serious aggregation of CNTs during the cement hydration process.

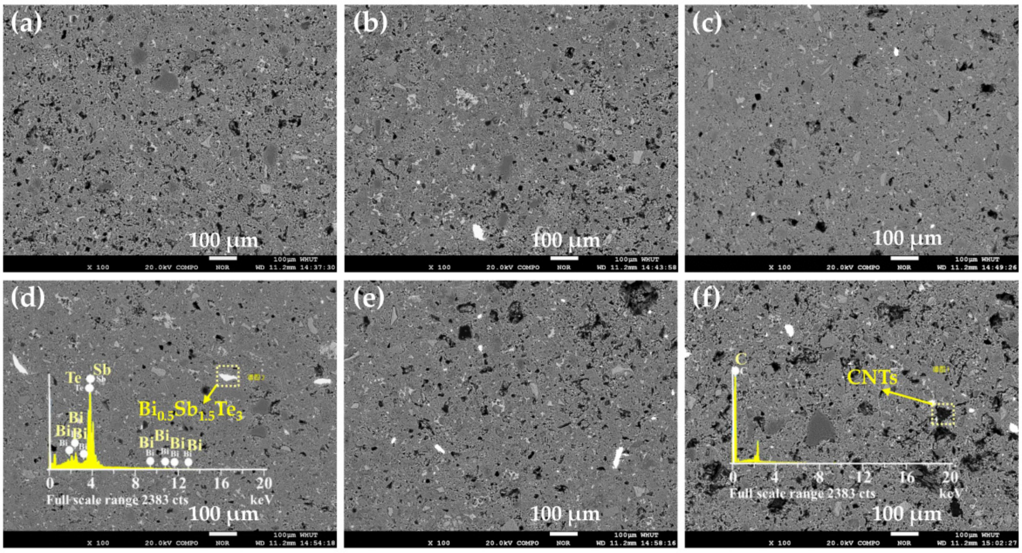

Figure 4. BEI photographs of $Bi_{0.5}Sb_{1.5}Te_3$/CNTs cement composites at different $Bi_{0.5}Sb_{1.5}Te_3$ contents: (**a**) x = 0.0 vol.%; (**b**) x = 0.2 vol.%; (**c**) x = 0.4 vol.%; (**d**) x = 0.6 vol.%; (**e**) x = 0.8 vol.%; and (**f**) x = 1.0 vol.%.

Figure 5 shows the backscattering electron image (BEI) and elemental maps of the $Bi_{0.5}Sb_{1.5}Te_3$/CNTs cement composites with $Bi_{0.5}Sb_{1.5}Te_3$ contents of 0.0 vol.% and 1.0 vol.%. The C-rich areas can be found in Figure 5b,e, suggesting that these areas contain the CNTs phase. Te-rich areas can be found in Figure 5f, indicating that these areas contain $Bi_{0.5}Sb_{1.5}Te_3$. For the sample without $Bi_{0.5}Sb_{1.5}Te_3$ particles, C is uniformly distributed, as shown in Figure 5b. However, when the content of $Bi_{0.5}Sb_{1.5}Te_3$ is 1.0 vol.%, the distribution of the CNTs in $Bi_{0.5}Sb_{1.5}Te_3$/CNTs cement composites become inhomogeneous, as shown in Figure 5e. This further reveals that the excessive $Bi_{0.5}Sb_{1.5}Te_3$ particles can lead to the aggregation of CNTs during hydration reaction.

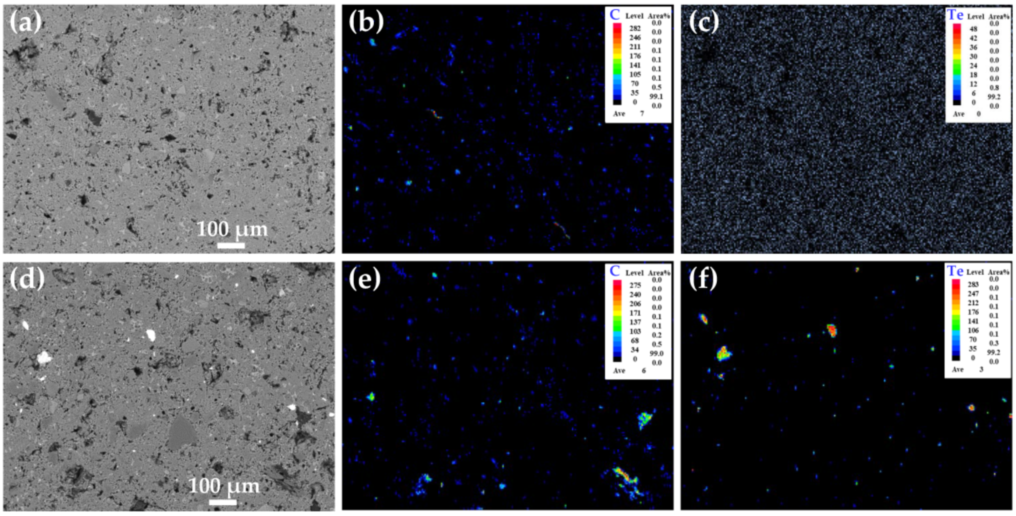

Figure 5. (**a**) BEI of $Bi_{0.5}Sb_{1.5}Te_3$/CNTs cement composites at 0.0 vol.% $Bi_{0.5}Sb_{1.5}Te_3$. The corresponding elemental maps are shown in (**b**) C and (**c**) Te; (**d**) BEI of of $Bi_{0.5}Sb_{1.5}Te_3$/CNTs cement composites at 1.0 vol.% $Bi_{0.5}Sb_{1.5}Te_3$. The corresponding elemental maps are shown in (**e**) C and (**f**) Te.

3.2. TE Properties of $Bi_{0.5}Sb_{1.5}Te_3$/CNTs Cement Composites

Figure 6a displays the electrical conductivity of $Bi_{0.5}Sb_{1.5}Te_3$/CNTs cement composites at different $Bi_{0.5}Sb_{1.5}Te_3$ contents. It can be seen that the σ increases with the increase in the $Bi_{0.5}Sb_{1.5}Te_3$ content. The sample with 1.0 vol.% $Bi_{0.5}Sb_{1.5}Te_3$ exhibits the largest σ value, which increases by 284 times compared to the sample without $Bi_{0.5}Sb_{1.5}Te_3$.

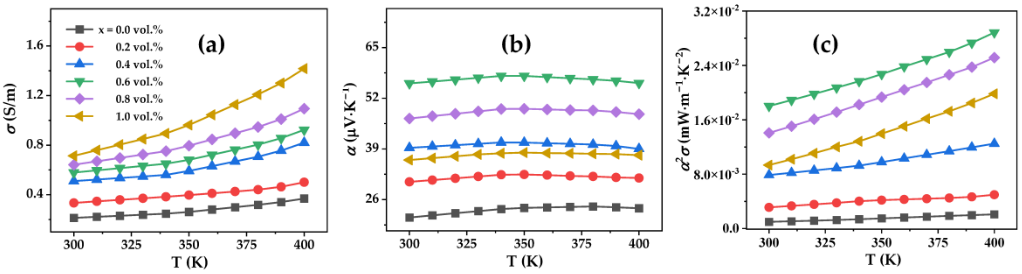

Figure 6. Temperature dependences of (**a**) electrical conductivity, (**b**) Seebeck coefficient, (**c**) power factor for the $Bi_{0.5}Sb_{1.5}Te_3$/CNTs cement composites.

The α of $Bi_{0.5}Sb_{1.5}Te_3$/CNTs cement composites are shown in Figure 6b. The positive α values indicate that the majority of the carriers of the $Bi_{0.5}Sb_{1.5}Te_3$/CNTs cement composites are holes, exhibiting p-type conduction. α first increased and then decreased in the temperature range of 300 K to 400 K as the content of $Bi_{0.5}Sb_{1.5}Te_3$ increased. The first increase in α of the samples means that the $Bi_{0.5}Sb_{1.5}Te_3$ multi-scale particles have a positive effect on enhancing the electrical transport properties of CNTs-reinforced cement composites. However, the α of the samples decreased with further increases in the

$Bi_{0.5}Sb_{1.5}Te_3$ contents. Combining the evolution features of microstructure from BEI results, the CNTs are uniformly dispersed at lower $Bi_{0.5}Sb_{1.5}Te_3$ contents, but accumulate together for the samples with the $Bi_{0.5}Sb_{1.5}Te_3$ contents of 0.8 vol.% and 1.0 vol.%. We believe that the decrease in α at the $Bi_{0.5}Sb_{1.5}Te_3$ contents of 0.8 vol.% and 1.0 vol.% comes from a positive effect of CNTs aggregation. The sample with 0.6 vol.% $Bi_{0.5}Sb_{1.5}Te_3$ shows the largest α of 40.66 μV/K at 350 K.

The power factor ($\alpha^2\sigma$) is plotted as a function of the $Bi_{0.5}Sb_{1.5}Te_3$ content (Figure 6c), which is calculated via the measured electrical conductivity and Seebeck coefficient. A dramatic enhancement in $\alpha^2\sigma$ is obtained in the sample with the 0.6 vol.% $Bi_{0.5}Sb_{1.5}Te_3$ at 400 K due to the remarkable increase in α and σ. This indicates that optimizing the doping content of $Bi_{0.5}Sb_{1.5}Te_3$ particles may effectively improve the electrical transport properties of $Bi_{0.5}Sb_{1.5}Te_3$/CNTs cement composites.

The κ of $Bi_{0.5}Sb_{1.5}Te_3$/CNTs cement composites are shown in Figure 7a. The κ of $Bi_{0.5}Sb_{1.5}Te_3$/CNTs cement composites first increases with the increase in the content of $Bi_{0.5}Sb_{1.5}Te_3$. However, the κ decreases with further increases in the content of $Bi_{0.5}Sb_{1.5}Te_3$ in the range of 0.6 vol.% to 1.0 vol.%, revealing that excessive $Bi_{0.5}Sb_{1.5}Te_3$ particles could lead to a lower κ.

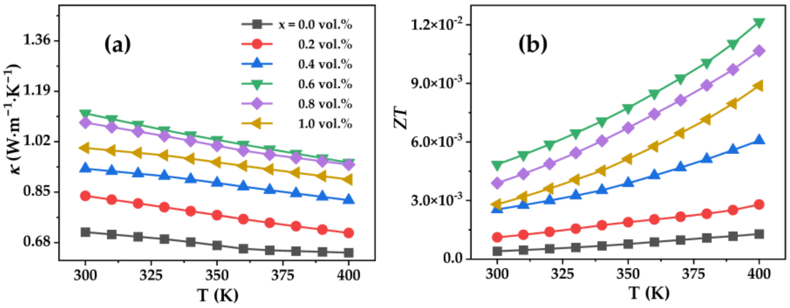

Figure 7. Temperature dependences of (**a**) thermal conductivity, (**b**) ZT for the $Bi_{0.5}Sb_{1.5}Te_3$/CNTs cement composites.

As a result, the ZT values (Figure 7b) first increases and then decreases with increases in the content of $Bi_{0.5}Sb_{1.5}Te_3$. The largest ZT reaches 1.2×10^{-2} at 400 K for the $Bi_{0.5}Sb_{1.5}Te_3$/CNTs co-reinforced cement composites at 0.6 vol.% $Bi_{0.5}Sb_{1.5}Te_3$, increasing by 842 times compared to the sample without $Bi_{0.5}Sb_{1.5}Te_3$ particles. The dramatic enhancement in the ZT values is obtained in the sample with 0.6 vol.% $Bi_{0.5}Sb_{1.5}Te_3$ due to the remarkable increase in σ and α. This work demonstrates that the addition of multi-scale $Bi_{0.5}Sb_{1.5}Te_3$ particles is an effective approach to enhance the TE performance of CNTs-reinforced cement composites.

3.3. Evaluation of $Bi_{0.5}Sb_{1.5}Te_3$/CNTs Cement Composites in Energy Harvesting from the Pavement

To demonstrate the potential application of the $Bi_{0.5}Sb_{1.5}Te_3$/CNTs co-reinforced cement composites, we measure the power generation performance of $Bi_{0.5}Sb_{1.5}Te_3$/CNTs cement composites at 0.6 vol% $Bi_{0.5}Sb_{1.5}Te_3$ with the size of $2.5 \times 3.5 \times 12\ mm^3$.

Figure 8a shows temperature difference (ΔT) dependences of the generated open-circuit voltage (Vo) for $Bi_{0.5}Sb_{1.5}Te_3$/CNTs cement composites at 0.6 vol.% $Bi_{0.5}Sb_{1.5}Te_3$, where the cold-side temperature (T_C) remains at 295.7 K. When the ΔT increases to 288 K and 303 K, the Vo is about 2.0 mV and 4.4 mV, respectively. Figure 8b demonstrates the work current (I) and power output (P) as a function of work voltage (V) under a ΔT of 19.1 K. The linear variation of I and the parabolic variation of P as a function of V represent a typical feature of power generators. The largest power output reaches 0.002 μW for the sample. The theoretical maximum power density P_d is estimated according to the equations $P_d = P/V$, where P_{max} is the maximum power output and V is the volume of the samples. From the above results, the P_d of $Bi_{0.5}Sb_{1.5}Te_3$/CNTs cement composites at 0.6 vol.% $Bi_{0.5}Sb_{1.5}Te_3$ is about 19 mW m^{-3} when the ΔT is 19.1 K.

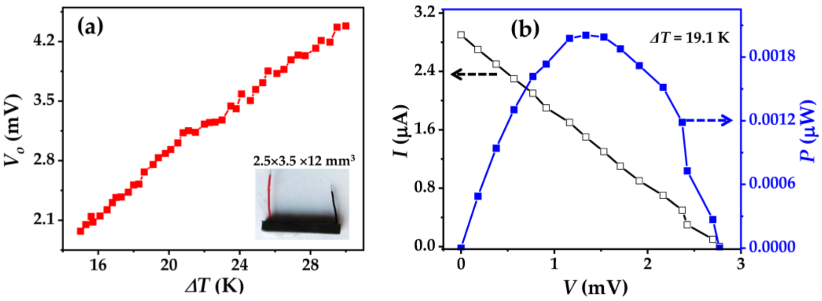

Figure 8. Power generation of $Bi_{0.5}Sb_{1.5}Te_3$/CNTs cement composites at 0.6 vol.% $Bi_{0.5}Sb_{1.5}Te_3$. (**a**) temperature difference (ΔT) dependences of open-circuit voltage (Vo) and (**b**) work voltage (V) dependences of work current (I) and power output (P) at a ΔT of 19.1 K.

The P_{max} value of $Bi_{0.5}Sb_{1.5}Te_3$/CNTs co-reinforced cement composites is not higher, but the amount of cement-related infrastructure on the earth is huge. For instance, when the temperature reduction in $Bi_{0.5}Sb_{1.5}Te_3$/CNTs co-reinforced cement concrete pavements of 1 km in length, 10 m in width and 20 cm in depth is 19.1 K, the generated electricity remains at about 38 W. With further development of TE cement, the power output of TE cement concrete pavements is likely to be enhanced, which will further promote the application of TE technology in harvesting green electricity.

4. Discussions

4.1. Conducting Behavior of $Bi_{0.5}Sb_{1.5}Te_3$/CNTs Co-Reinforced Cement Composites

To clarify the conductive behavior of $Bi_{0.5}Sb_{1.5}Te_3$/CNTs co-reinforced cement composites, we investigate the C and Te elemental maps of the samples with 1.0 vol.% $Bi_{0.5}Sb_{1.5}Te_3$. The analyses are carried out by extracting C and Te distribution from their elemental maps, and then overlaying Te onto C to explore the conductive network, as shown in Figure 9. When CNTs are dispersed in cement materials, some CNTs come into contact with each other and form a local conductive network. After addition of multi-scale $Bi_{0.5}Sb_{1.5}Te_3$ particles, a tortuous but better conductive path can be formed between $Bi_{0.5}Sb_{1.5}Te_3$ and CNTs. Therefore, the significant enhancement in the electrical conductivity should be attributed to the occurrence of a better conductive network in $Bi_{0.5}Sb_{1.5}Te_3$/CNTs co-reinforced cement composites.

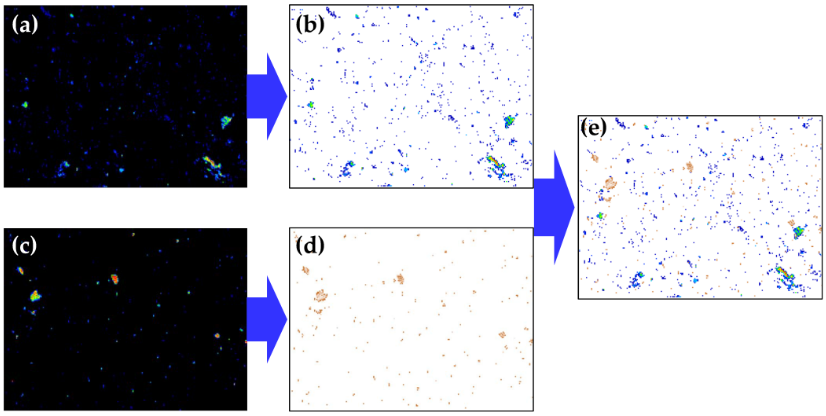

Figure 9. The elemental mapping of (**a**) C and (**c**) Te of $Bi_{0.5}Sb_{1.5}Te_3$/CNTs cement composites at 1.0 vol.% $Bi_{0.5}Sb_{1.5}Te_3$. The corresponding elemental distributions, which were extracted from (**a**,**c**), are shown in (**b**,**d**). The elemental distribution of (**d**) Te is overlayed on the elemental distribution of (**b**) C to explore the conductive network with (**e**) C+Te.

4.2. Multi-Scale $Bi_{0.5}Sb_{1.5}Te_3$ Particles and Its Effects

Figure 10 shows the SEM images and EDS of $Bi_{0.5}Sb_{1.5}Te_3$/CNTs co-reinforced cement composites at 0.6 vol.% $Bi_{0.5}Sb_{1.5}Te_3$. It can be seen that the fracture section of the samples is compact. The enlarged SEM image clearly indicates that a great variety of tube-like CNTs are distributed in the rough grain boundary of $Bi_{0.5}Sb_{1.5}Te_3$ in cement composites, as shown in Figure 10b. The randomly bridged $Bi_{0.5}Sb_{1.5}Te_3$ and CNTs in the co-reinforced cement composites can lead to a significant enhancement in the electrical conductivity via a better conductive network. The rough surfaces are very beneficial, decreasing the thermal conductivity by increasing the boundary scattering of phonons. In addition, the multiscale microstructures will serve as energy-dependent selective scattering centers to filter the low-energy carriers and improve the α. Hu et al. [38] observed the same phenomenon in the Bi_2Te_3-based TE materials. Thus, it can be concluded that the tunneling effect and phonons scattering in the co-reinforced cement composites are enhanced because of the presence of randomly arranged multi-scale $Bi_{0.5}Sb_{1.5}Te_3$ particles, which arises from enhanced conductive network, energy-dependent selective scattering and phonon scattering in the $Bi_{0.5}Sb_{1.5}Te_3$/CNTs-co-reinforced cement composites.

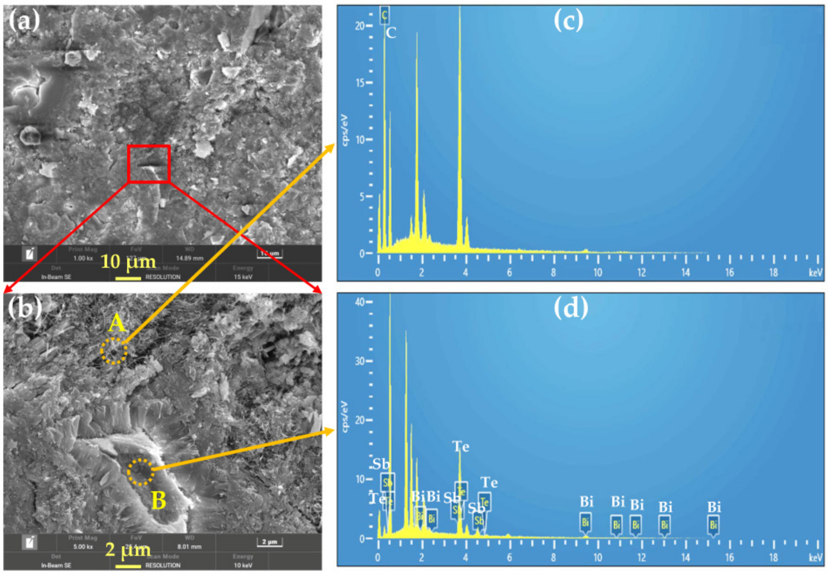

Figure 10. (**a**) SEM image and (**b**) enlarged SEM image of $Bi_{0.5}Sb_{1.5}Te_3$/CNTs co-reinforced cement composites at 0.6 vol.% $Bi_{0.5}Sb_{1.5}Te_3$. (**c**,**d**) EDS patterns of the point A and B in (**b**), respectively.

4.3. Mechanism of the Enhancement in TE Performance of $Bi_{0.5}Sb_{1.5}Te_3$/CNTs Co-Reinforced Cement Composites

To better understand the mechanism of enhanced TE performance of CNTs reinforced cement composites with multi-scale $Bi_{0.5}Sb_{1.5}Te_3$ particles, we draw up the schematic shown in Figure 11. For cement composites, the electrical conduction involves ions, electrons, and/or holes. The main conduction of pure cement is ionic with free water solution, including Ca^{2+}, Na^+, K^+, OH^-, $SO_4{}^{2-}$. In this work, the cured cement composites were dried for at 105 °C for 12 h before the test. Under such circumstances, the cement paste is almost an insulating material due to no free water. When CNTs are dispersed in cement materials, some CNTs come into contact with each other to form a conductive network. The carriers (electrons and holes) will move along the conductive network or pass through the adjacent disconnected CNTs based on tunneling theory [39], which leads to an increment in σ of CNTs-reinforced cement composites. After addition of multi-scale $Bi_{0.5}Sb_{1.5}Te_3$ particles, a tortuous but better conductive network can be formed in $Bi_{0.5}Sb_{1.5}Te_3$ and CNTs. Hence, the electrical conductivity of $Bi_{0.5}Sb_{1.5}Te_3$/CNTs co-reinforced cement composites is further increased.

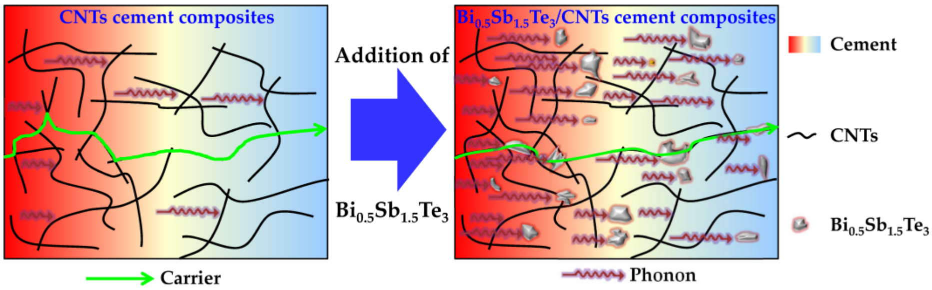

Figure 11. A schematic mechanism for multi-scale $Bi_{0.5}Sb_{1.5}Te_3$ particles in enhancing the TE performance of CNTs reinforced cement composites.

Moreover, the multi-scale $Bi_{0.5}Sb_{1.5}Te_3$ particles can enhance the low-energy electron filtering effect, thus improving the α of co-reinforced cement composites. However, the excessive $Bi_{0.5}Sb_{1.5}Te_3$ particles lead to the aggregation of CNTs, thus lowering the energy-filtering effect of CNTs and α of co-reinforced cement composites. Additionally, for the multi-scale $Bi_{0.5}Sb_{1.5}Te_3$ particles, there are a number of interfaces that can scatter the phonon, and thus lower the κ of $Bi_{0.5}Sb_{1.5}Te_3$/CNTs co-reinforced cement composites. Consequently, the multi-scale $Bi_{0.5}Sb_{1.5}Te_3$ particles embedded in the CNTs-reinforced cement composites increase σ and α and lower κ. The increased ZT of $Bi_{0.5}Sb_{1.5}Te_3$/CNTs co-reinforced cement composites should be responsible for the shorter conductive network, energy filtering and interfaces scattering by the $Bi_{0.5}Sb_{1.5}Te_3$ multi-scale particles.

5. Conclusions

In this paper, a series of $Bi_{0.5}Sb_{1.5}Te_3$/CNTs cement composites were prepared via a co-reinforced method, and their TE properties were systematically investigated. It was discovered that the $Bi_{0.5}Sb_{1.5}Te_3$/CNTs-co-reinforced cement composites with 0.6 vol.% $Bi_{0.5}Sb_{1.5}Te_3$ exhibit the highest ZT value of 1.2×10^{-2}. The enhanced ZT value mainly originates from the formation of shorter conductive network, increased energy filtering, and defects scattering by multi-scale $Bi_{0.5}Sb_{1.5}Te_3$ particles. The power output of this sample with the size of $2.5 \times 3.5 \times 12$ mm^3 reaches 0.002 μW at a temperature difference of 19.1 K. This work introduces a successful route to develop high-performance TE cement, which can be extended to harvest thermal energy in pavements.

Author Contributions: Software, data curation, writing—original draft preparation, writing—review and editing, funding acquisition, H.Z.; methodology, investigation, H.L.; writing—review and editing, formal analysis, G.Q.; writing—review and editing, validation, P.X., H.Y. and J.C.; conceptualization and visualization, J.Z. All authors have read and agreed to the published version of the manuscript.

Funding: This work was supported by the National Natural Science Foundation of China (52008043, 51778071), the Hunan Province Natural Science Foundation of China (2020JJ5598), the science and technology innovation Program of Hunan Province (2020RC4048), the China Postdoctoral Science Foundation (2019M652747, 2020T130570) and the Open Fund (kfj190105, kfj210701) of the National Engineering Laboratory of Highway Maintenance Technology (Changsha University of Science and Technology).

Institutional Review Board Statement: Not applicable.

Informed Consent Statement: Not applicable.

Data Availability Statement: Not applicable.

Acknowledgments: EPMA and FESEM experiments were performed at the Center for Materials Research and Testing of Wuhan University of Technology. Thermoelectric performance measurements were performed at State Key Laboratory of Advanced Technology for Materials Synthesis and Processing of Wuhan University of Technology. The authors are grateful to X.L. Nie, and W.Y. Zhao from Wuhan University of Technology for their fruitful collaborations.

Conflicts of Interest: The authors declare no conflict of interest.

References

1. Brito, J.D.; Kurda, R. The past and future of sustainable concrete: A critical review and new strategies on cement-based materials. *J. Clean. Prod.* **2021**, *281*, 123558. [CrossRef]
2. Sharma, M.; Bishnoi, S.; Martirena, F.; Scrivener, K. Limestone calcined clay cement and concrete: A state-of-the-art review. *Cem. Concr. Res.* **2021**, *149*, 106564. [CrossRef]
3. Biernacki, J.J.; Bullard, J.W.; Sant, G.; Brown, K.; Glasser, F.P.; Jones, S.; Ley, T.; Livingston, R.; Nicoleau, L.; Olek, J.; et al. Cements in the 21(st) century: Challenges, perspectives, and opportunities. *J. Am. Ceram. Soc.* **2017**, *100*, 2746–2773. [CrossRef] [PubMed]
4. Anupam, B.R.; Sahoo, U.C.; Chandrappa, A.K.; Rath, P. Emerging technologies in cool pavements: A review. *Constr. Build. Mater.* **2021**, *299*, 123892. [CrossRef]
5. Qin, Y.H. A review on the development of cool pavements to mitigate urban heat island effect. *Renew. Sust. Energy Rev.* **2015**, *52*, 445–459. [CrossRef]
6. Wang, A.; Zhang, Z.; Lei, X.; Xia, Y.; Sun, L. All-weather thermal simulation methods for concrete maglev bridge based on structural and meteorological monitoring data. *Sensors* **2021**, *21*, 5789. [CrossRef]
7. Vujovic, S.; Haddad, B.; Karaky, H.; Sebaibi, N.; Boutouil, M. Urban heat island: Causes, consequences, and mitigation measures with emphasis on reflective and permeable pavements. *Civ. Eng.* **2021**, *2*, 459–484. [CrossRef]
8. Hwang, R.L.; Lin, T.P.; Lin, F.Y. Evaluation and mapping of building overheating risk and air conditioning use due to the urban heat island effect. *J. Build. Eng.* **2020**, *32*, 101726. [CrossRef]
9. Delgado-Alvarado, E.; Elvira-Hernández, E.A.; Hernández-Hernández, J.; Huerta-Chua, J.; Vázquez-Leal, H.; Martínez-Castillo, J.; García-Ramírez, P.J.; Herrera-May, A.L. Recent progress of nanogenerators for green energy harvesting: Performance, applications, and challenges. *Nanomaterials* **2022**, *12*, 2549. [CrossRef]
10. Singh, V.P.; Kumar, M.; Srivastava, R.S.; Vaish, R. Thermoelectric energy harvesting using cement-based composites: A review. *Mater. Today Energy* **2021**, *21*, 100714. [CrossRef]
11. Al Musleh, M.; Topriska, E.V.; Jenkins, D.; Owens, E. Thermoelectric generator characterization at extra-low-temperature difference for building applications in extreme hot climates: Experimental and numerical study. *Energy Build.* **2020**, *225*, 110285. [CrossRef]
12. Gholikhani, M.; Roshani, H.; Dessouky, S.; Papagiannakisa, A.T. A critical review of roadway energy harvesting technologies. *Appl. Energy* **2020**, *261*, 114388. [CrossRef]
13. Ma, Z.; Wei, J.T.; Song, P.S.; Zhang, M.L.; Yang, L.L.; Ma, J.; Liu, W.; Yang, F.H.; Wang, X.D. Review of experimental approaches for improving zT of thermoelectric materials. *Mater. Sci. Semicon. Proc.* **2021**, *121*, 105303. [CrossRef]
14. Sun, M.; Li, Z.; Mao, Q.; Shen, D. Thermoelectric percolation phenomena in carbon fiber-reinforced concrete. *Cem. Concr. Res.* **1998**, *28*, 1707–1712. [CrossRef]
15. Vareli, I.; Tzounis, L.; Tsirka, K.; Kavvadias, I.E.; Tsongas, K.; Liebscher, M.; Elenas, A.; Gergidis, L.N.; Barkoulaa, N.; Paipetis, A.S. High-performance cement/SWCNT thermoelectric nanocomposites and a structural thermoelectric generator device towards large-scale thermal energy harvesting. *J. Mater. Chem. C* **2021**, *9*, 14421–14438. [CrossRef]
16. Wang, X.Y.; Dong, S.F.; Ashour, A.; Han, B.G. Energy-harvesting concrete for smart and sustainable infrastructures. *J. Mater. Sci.* **2021**, *56*, 16243–16277. [CrossRef]
17. Ji, T.; Zhang, X.; Li, W.H. Enhanced thermoelectric effect of cement composite by addition of metallic oxide nanopowders for energy harvesting in buildings. *Constr. Build. Mater.* **2016**, *115*, 576–581. [CrossRef]
18. Ghosh, S.; Harish, S.; Rocky, K.A.; Ohtaki, M.; Saha, B.B. Graphene enhanced thermoelectric properties of cement based composites for building energy harvesting. *Energy Build.* **2019**, *202*, 109419. [CrossRef]
19. Ji, T.; Zhang, X.Y.; Zhang, X.; Zhang, Y.J. Effect of manganese dioxide nanorods on the thermoelectric properties of cement composites. *J. Mater. Civ. Eng.* **2018**, *30*, 04018224. [CrossRef]
20. Wen, S.H.; Chung, D.D.L. Enhancing the Seebeck effect in carbon fiber-reinforced cement by using intercalated carbon fibers. *Cem. Concr. Res.* **2000**, *30*, 1295–1298. [CrossRef]
21. Bahar, D.; Salih, Y. Thermoelectric behavior of carbon fiber reinforced lightweight concrete with mineral admixtures. *New Carbon Mater.* **2008**, *23*, 21–24. [CrossRef]
22. Davoodabadi, M.; Vareli, I.; Liebscher, M.; Tzounis, L.; Sgarzi, M.; Paipetis, A.S.; Yang, J.; Cuniberti, G.; Mechtcherine, V. Thermoelectric energy harvesting from single-walled carbon nanotube alkali-activated nanocomposites produced from industrial waste materials. *Nanomaterials* **2021**, *11*, 1095. [CrossRef] [PubMed]
23. Shi, T.; Li, Z.X.; Guo, J.; Gong, H.; Gu, C.P. Research progress on CNTs/CNFs-modified cement-based composites—A review. *Constr. Build. Mater.* **2019**, *202*, 290–307. [CrossRef]
24. García-Macías, E.; D'Alessandro, A.; Castro-Triguero, R.; Pérez-Mira, D.; Ubertini, F. Micromechanics modeling of the electrical conductivity of carbon nanotube cement-matrix composites. *Compos. Part B Eng.* **2017**, *108*, 451–469. [CrossRef]
25. Zuo, J.Q.; Yao, W.; Wu, K.R. Seebeck effect and mechanical properties of carbon nanotube-carbon fiber/cement nanocomposites. *Fuller. Nanotub. Carbon Nanostructures* **2014**, *23*, 383–391. [CrossRef]
26. Wei, J.; Li, X.T.; Wang, Y.; Chen, B.; Qiao, S.S.; Zhang, Q.; Xue, F. Record high thermoelectric performance of expanded graphite/carbon fiber cement composites enhanced by ionic liquid 1-butyl-3-methylimidazolium bromide for building energy harvesting. *J. Mater. Chem. C* **2021**, *9*, 3682–3691. [CrossRef]

27. Wei, J.; Zhang, Q.; Zhao, L.L.; Hao, L.; Yang, C.L. Enhanced thermoelectric properties of carbon fiber reinforced cement composites. *Ceram. Int.* **2016**, *42*, 11568–11573. [CrossRef]
28. Wei, J.; Wang, Y.; Li, X.T.; Jia, Z.Y.; Qiao, S.S.; Jiang, Y.C.; Zhou, Y.Q.; Miao, Z.; Gao, D.M.; Zhang, H. Dramatically improved thermoelectric properties by defect engineering in cement-based composites. *ACS Appl. Mater. Interfaces* **2021**, *13*, 3919–3929. [CrossRef]
29. Wei, J.; Hao, L.; He, G.P.; Yang, C.L. Enhanced thermoelectric effect of carbon fiber reinforced cement composites by metallic oxide/cement interface. *Ceram. Int.* **2014**, *40*, 8261–8263. [CrossRef]
30. Liu, X.Y.; Liao, G.; Zuo, J.Q. Enhanced thermoelectric properties of carbon fiber-reinforced cement composites (CFRCs) utilizing Bi_2Te_3 with three doping methods. *Fuller. Nanotub. Carbon Nanostructures* **2021**, *29*, 295–303. [CrossRef]
31. Ghosh, S.; Harish, S.; Ohtaki, M.; Saha, B.B. Thermoelectric figure of merit enhancement in cement composites with graphene and transition metal oxides. *Mater. Today Energy* **2020**, *18*, 100492. [CrossRef]
32. Qiu, W.B.; He, H.; Wang, Z.S.; Hu, Q.J.; Cui, X.D.; Wang, Z.G.; Zhang, Y.; Gu, L.; Yang, Y.X.; Zhao, L.W.; et al. Enhancing the figure of merit of n-type PbTe materials through multi-scale graphene induced interfacial engineering. *Nano Today* **2021**, *39*, 101176. [CrossRef]
33. Zhang, C.C.; Zhao, Y.; Gu, P.; Peng, L.M. Thermoelectric performance in pseudo-ternary $(PbTe)_{0.95\text{-}x}(Sb_2Se_3)_x(PbS)_{0.05}$ system with ultra-low thermal conductivity via multi-scale phonon scattering. *Curr. Appl. Phys.* **2020**, *20*, 1008–1012. [CrossRef]
34. Hori, T.; Shiomi, J. Tuning phonon transport spectrum for better thermoelectric materials. *Sci. Technol. Adv. Mater.* **2019**, *20*, 10–25. [CrossRef]
35. Pei, J.; Cai, B.W.; Zhuang, H.L.; Li, J.F. Bi_2Te_3-based applied thermoelectric materials: Research advances and new challenges. *Natl. Sci. Rev.* **2020**, *7*, 1856–1858. [CrossRef]
36. Hao, F.; Qiu, P.F.; Tang, Y.S.; Bai, S.Q.; Xing, T.; Chu, H.; Zhang, Q.H.; Lu, P.; Zhang, T.S.; Ren, D.D.; et al. High efficiency Bi_2Te_3-based materials and devices for thermoelectric power generation between 100 and 300 °C. *Energy Environ. Sci.* **2016**, *9*, 3120–3127. [CrossRef]
37. Baneviien, V.; Malaikien, J. The synergistic effect of secondary raw materials and nano additive on the properties of cement matrix. *IOP Conf. Ser. Mater. Sci. Eng.* **2020**, *960*, 022038. [CrossRef]
38. Hu, L.P.; Wu, H.J.; Zhu, T.J.; Fu, C.G.; He, J.Q.; Ying, P.J.; Zhao, X.B. Tuning multiscale microstructures to enhance thermoelectric performance of *n*-type bismuth-telluride-based solid solutions. *Adv. Energy Mater.* **2015**, *5*, 1500411. [CrossRef]
39. Wang, L.N.; Aslani, F. A review on material design, performance, and practical application of electrically conductive cementitious composites. *Constr. Build. Mater.* **2019**, *229*, 116892. [CrossRef]